Journal of Materials Chemistry A

PAPER

View Article Online
View Journal | View Issue

Cite this: J. Mater. Chem. A, 2019, 7, 19846

Extended layer-by-layer Madelung potential analysis of layered oxyhalide photocatalysts and other layered systems†

Daichi Kato, [a] Ryu Abe *[ab] and Hiroshi Kageyama *[ab]

A recent study on Bi_4NbO_8Cl and related Bi-based layered oxyhalide photocatalysts using a layer-by-layer Madelung potential (L^2MP) analysis with a sphere model revealed that oxide anions in the fluorite-type slab of Bi_4NbO_8Cl are electrostatically destabilized by the 2nd nearest sublayer composed of the apical oxygen of the perovskite slab. Here we provide an extended L^2MP analysis of Bi-based layered oxyhalides using a modified (square-prism) model and apply it to other layered compounds. It is found that consideration of up to the 3rd nearest sublayer is necessary to account for the nearly equal valence band maximum between Bi_2GdO_4X and Bi_4NbO_8Cl. Additionally, BiOX and Bi_2GdO_4X show a distinct X-dependence of the Madelung site potential of oxide anions. The L^2MP analysis of Bi_2WO_6, $Sr_3Sc_2Cu_2S_2O_5$ and $Sr_2ScCuSO_3$ revealed a sizable contribution of distant layers to their electrostatic potentials. This study demonstrates that this method can be applied to a wide range of layered materials and serves as a powerful guide toward finding composition and layer stacking sequences suitable for photocatalysis and other functions.

Received 17th May 2019
Accepted 31st July 2019

DOI: 10.1039/c9ta05201a

rsc.li/materials-a

Introduction

There is an intimate relationship between the crystal structures of extended solids and the properties they exhibit. One of the key descriptors for ionic solids is the Madelung site potential, or the sum of the electrostatic potentials created at a specific crystallographic site by surrounding ions. The Madelung site potential was used to explain band formation in ionic solids such as NaCl, ZnS and $SrTiO_3$ in the 1960–70's,[1–3] and high-T_c cuprate superconductors in the 1980–90's.[4–6] In recent years, there is a renewed interest in using the Madelung site potential, for example, valence skip fluctuation in $BaBiO_3$,[7] the surface defect behaviour of metal oxides,[8] and the band location in eight TiO_2 polymorphs.[9,10] Despite the long-range nature of Coulomb interactions, the difference in Madelung site potential is mainly explained by the local coordination environment and less attention appears to be paid to distant ions.[4,9,10]

Recently, we have developed a series of layered bismuth oxyhalide photocatalysts, Bi_4NbO_8Cl[11] and its derivatives,[12–14] as highly efficient visible-light responsive photocatalysts for water splitting with extraordinary stability against self-oxidative deactivation by photo-generated holes. The photocatalytic stability of Bi_4NbO_8Cl and its narrow band gap (2.39 eV) are attributed to the presence of O 2p orbitals at the valence band maximum (VBM) rather than Cl 3p orbitals. The unusual upward shift of oxygen 2p bands is understood in terms of the Madelung site potential of anions[15] as well as the Bi lone pair effect.[16] In particular, Madelung site potential calculation revealed that the oxide anion in the fluorite-type blocks of Bi_4NbO_8X (X = Cl, Br) (Fig. 1b) and Bi_2GdO_4X (Fig. 1c) has a lower Madelung site potential in comparison with BiOX (Fig. 1a),

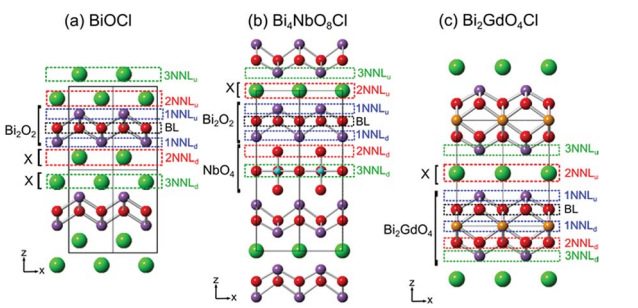

Fig. 1 Crystal structures of (a) BiOX (X = Cl, Br, I), (b) Bi_4NbO_8X (X = Cl, Br) and (c) Bi_2GdO_4X (X = Cl, Br, I). The fluorite-derived basal layer (BL) and its neighboring sublayers (*n*-th nearest-neighbor layer; *n*NNL) are indicated. Purple, red, yellow-green and blue spheres, respectively, represent Bi, O, halogen (X) and Nb atoms. The non-distorted structure is given for (b). For each, the unit cell is indicated by solid black lines.

[a]Department of Energy and Hydrocarbon Chemistry, Graduate School of Engineering, Kyoto University, Nishikyo-ku, Kyoto 615-8510, Japan. E-mail: ryu-abe@scl.kyoto-u.ac.jp; kage@scl.kyoto-u.ac.jp

[b]CREST, Japan Science and Technology Agency (JST), Kawaguchi, Saitama 332-0012, Japan

† Electronic supplementary information (ESI) available: Detailed discussion on electrostatic potential from surrounding sub-layers in BiOCl and crystal structures and the value of Madelung site potential (PDF). See DOI: 10.1039/c9ta05201a

leading to the upward shift of the VBM. To further clarify the role and contribution of each layer, we subsequently developed a layer-by-layer Madelung potential (L^2MP) analysis and found that the destabilization of the oxide anion in Bi_4NbO_8X and Bi_2GdO_4X is due to strong repulsive interactions from the oxide anions in the 2nd nearest-neighbor sublayer (2NNL; Fig. 1),[15] as shown in Fig. 2 (left) and S3.†

Given the long-range nature of Coulomb interactions, further sublayers may also affect the valence band structures of these Bi-based oxyhalides. However, the sphere model (Fig. 3a), where the electrostatic potentials of ions within $R = 4$ Å from the oxide anion in the fluorite-type layers were taken into consideration, cannot properly extract the contribution of the distant sublayers such as the 3NNL. In addition, the effect of halogens (X) on their Madelung potential has not been addressed, in spite of the fact that many isostructural (Cl, Br, and I) oxyhalides have different band gaps.

The aforementioned compounds are just a few examples of more than 100 oxyhalides with the Bi_2O_2 fluorite layer.[17] Furthermore, there are a number of modular compounds whose structures are built from slabs of a parent motif interleaved with other layers. Available building blocks include anti-fluorite, rock salt and perovskite layers to name only a few. Such a structural diversity in layered materials has resulted in a wide range of functional properties including superconductivity in cuprates,[18] FeAs- and BiS_2-based compounds,[19–21] secondary batteries in layered rock-salt oxides,[22] and transparent conductivity in Cu_2S_2-based compounds.[23,24] We thus expect that Madelung analysis could be applied to other layered systems toward obtaining desired photocatalytic activities and other functions.

This study aims to address these issues by including a wider range of ions for BiOX, Bi_4NbO_8X and Bi_2GdO_4X as well as other classes of layered materials. Two alternate models are employed for layer-by-layer Madelung potential (L^2MP) analysis by changing the size included in the calculation. This extended analysis revealed that a 3NN sublayer plays a crucial role in the valence band structures in Bi_2GdO_4X and Bi_4NbO_8Cl, while the origin of the X-dependence of the band gap is discussed. In addition, L^2MP analysis is also applied to Bi_2WO_6, $Sr_3Sc_2Cu_2S_2O_5$ and $Sr_2ScCuSO_3$ to investigate the impact of distant sublayers on their Madelung potential.

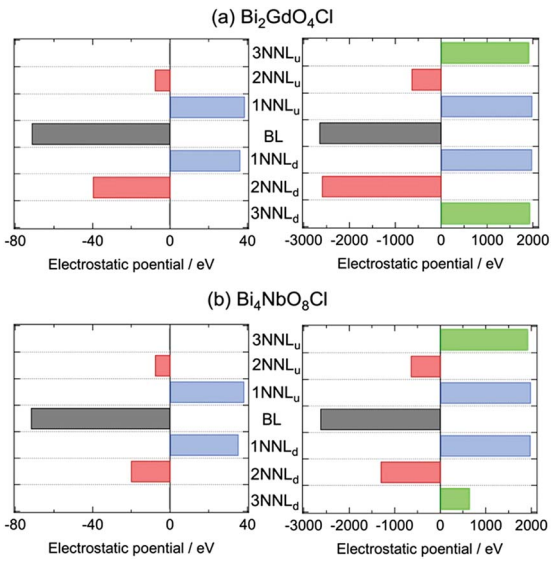

Fig. 2 Electrostatic potential at the oxygen site in the fluorite-type layer from adjacent sublayers of (a) Bi_2GdO_4Cl and (b) Bi_4NbO_8Cl. Calculation using (left) the sphere model[15] and (right) the square-prism model (this work) for $A = 200$ Å (Fig. 3). The non-distorted hypothetical structure was used for Bi_4NbO_8Cl.

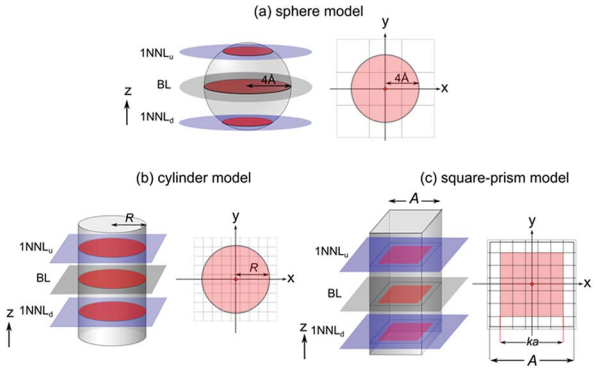

Fig. 3 Three models employed for calculating the electrostatic potential at the oxygen site in the BL from each sublayer: (a) sphere model,[15] (b) cylinder model, and (c) square-prism model. For each model, cations and anions within the red area are taken into consideration. On the right side of each panel, the unit cell is indicated in grey. The red area in the square-prism model shows that $-ka/2 \leq x, y \leq ka/2$ (where k is an odd number satisfying $ka \leq A \leq (k + 1)a$). The oxide anion in question is placed at the center of (a) sphere, (b) circle, and (c) square.

Methods

The electrostatic potential was calculated using the structural data reported in ref. 25–31. For Bi_4NbO_8Cl and Bi_2WO_6, non-distorted lattices were constructed, where the atomic coordinates of each atomic position were set to the average values of experimentally obtained structures, as shown in Tables S1 and S2.†[25,31] Structural optimization based on density functional theory (DFT) was performed for the hypothetical Bi_4NbO_8Cl structure using the Cambridge Serial Total Energy Package (CASTEP).[32] The energy was calculated using the PbEsol XC functional.[33] Cutoff energy and k-point grids were 630 eV and 4 × 4 × 1. As illustrated in Fig. 3, the following two models were used to estimate the electrostatic potential generated at the oxygen site in the fluorite-type Bi_2O_2 (or Bi_2GdO_4) slab from each sublayer. The first model (cylinder model) took account of the electrostatic interactions between the oxide anion at the center of a cylinder with a radius of R (Fig. 3b) and all other atoms in the cylinder. Another model (square-prism model) considered the electrostatic interaction between the oxide anion at the center of a square-prism with a side length of A (Fig. 3c) and all other atoms within $-ka/2 \leq x, y \leq ka/2$ (k is an odd number satisfying $ka \leq A \leq (k + 1)a$). The central oxygen was located at $(x, y) = (0, 0)$.

In calculating the Madelung site potential at the oxygen site, we fixed the value of R (cylinder model) or A (square-prism model) and changed the z-axis range. It is important to employ an electrically neutral domain to achieve reasonable convergence when the calculation range expands. For this reason, we have defined the charge-neutral sublayer set for $(m-1)c \leq |z| < mc$ (where $m = 1, 2, 3\ldots$) as U_1, U_2, U_3,…, U_m… (see Fig. S4†), and calculated the Madelung potential as a function of m.

The Madelung site potential of Bi_4NbO_8Cl with the distortion-free model was calculated by the Fourier method incorporated into the VESTA program.[34] The radius of an ionic sphere and the reciprocal-space range were, respectively, set at 1.8 Å and 3 $Å^{-1}$ after convergence of the Madelung site potentials with respect to these two parameters was checked.

Results and discussion

We first applied the two models to BiOCl and checked how the Madelung potential at the oxide anion of the BL from adjacent sublayers evolves and is converged into the theoretical value when the lateral size included in the calculation increases. In the cylinder model, the electrostatic potential as a function of m is largely affected by R (Fig. 4a) and the electrostatic potential did not approach the value previously obtained by the Fourier method based on the calculation in reciprocal space, which is probably because the electrical neutrality is not guaranteed in this model.[15,34] In the square-prism model, in contrast, the electrostatic potential converged rapidly with A (Fig. 4b). Regardless of the choice of A, the electrostatic potential monotonically decreased with m and quickly converged to the expected value of 20.8 eV (Fig. 4b).

These results indicate that the square-prism model is more appropriate, so this model was applied to other Bi-containing oxyhalides (Fig. 5). The electrostatic potential for $A = 200$ Å successfully converged to a value close to that obtained from the Fourier method: 21.9 eV for BiOBr, 23.7 eV for BiOI and 17.8 eV for Bi_2GdO_4Cl. As for Bi_4NbO_8Cl, we encountered a problem of conditional convergence[35] even for the square-prism model; due to the orthorhombic structure involving octahedral rotations (Fig. S2†), it was not possible to find an appropriate charge-neutral domain. Therefore, a non-distorted tetragonal structure ($P4/mmm$ space group) was constructed. The difference in lattice parameters before and after optimization of this hypothetical structure is 1.23% (Tables S1 and S3†), which is within the margin of error of DFT calculation using the PBEsol XC functional. Using this hypothetical structure, we obtained a Madelung site potential of 18.3 eV by the Fourier method for the oxygen site in the fluorite-type Bi_2O_2. This is similar to the values for the actual structure (O1: 18.9 eV, O2: 18.2 eV, O3: 18.3 eV, and O4: 17.5 eV),[15] suggesting that the presence of octahedral tilting does not significantly influence the Madelung site potential. The electrostatic potential at the oxygen site using the non-distorted model converged well to the value obtained by the Fourier method (Fig. 5).

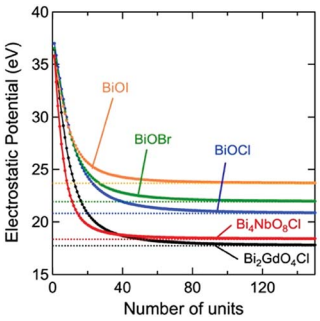

Fig. 5 Total electrostatic potential created at the oxygen site (in the fluorite-type layer) for BiOX, Bi_2GdO_4Cl and Bi_4NbO_8Cl and plotted with respect to the number of U_m. Madelung site potentials of the oxygen site obtained by the Fourier method (implemented in the VESTA program[34]) are shown by the dotted lines. The Madelung site potentials of BiOX and Bi_2GdO_4Cl are taken from a previous report,[15] while a non-distorted structure was used for Bi_4NbO_8Cl.

Fig. 6 shows the electrostatic potentials for BiOCl and Bi_2YO_4Cl from the BL, $1NNL_u$ and $2NNL_u$ plotted as a function of A. Because of common units (BL: $[O_2]$, 1NNL: [Bi] and 2NNL: [Cl]), the electrostatic potentials of each sublayer are almost the same. Moreover, the Madelung potential from each sublayer exhibits a linear dependence, with the slope ratio of BL : 1NNL : 2NNL = 4 : 3 : 1 corresponding to the ratio of the formal charge in each sublayer: $[O_2]^{4-}$, $[Bi]^{3+}$ and $[Cl]^{-}$ (see the ESI† for details).

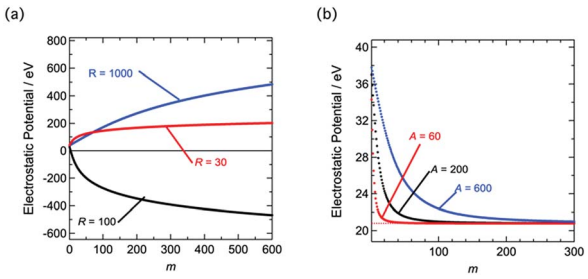

Fig. 4 The m dependence of the total electrostatic potential at the oxygen site of BiOCl calculated with (a) the cylinder model and (b) the square-prism model, for a fixed size of the circle ($R = 30$ Å, 100 Å and 1000 Å) and square ($A = 60$ Å, 200 Å and 600 Å). Madelung potential obtained by the Fourier method (corresponding to the infinite-size limit) is shown by the dotted red line in (b).

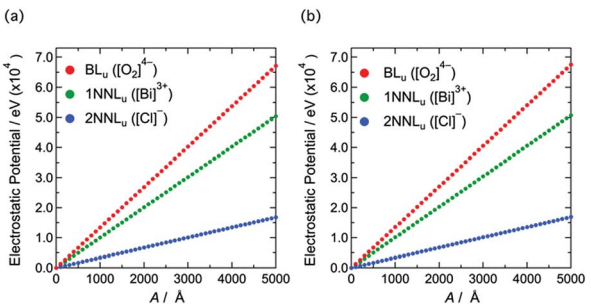

Fig. 6 The A dependence of the absolute value of electrostatic potential from the BL, $1NNL_u$ and $2NNL_u$ in (a) BiOCl and (b) Bi_2GdO_4Cl calculated using the square-prism model.

The sphere model, employed previously,[15] revealed that the Madelung site potential at the oxygen site in Bi_2O_2 slabs of Bi_4NbO_8Cl (18.2 eV on average) is smaller than that of BiOCl (20.8 eV), which was attributed to the smaller electrostatic potential generated by the $2NNL_d$ in Bi_4NbO_8Cl (−20.3 eV *vs.* −9.0 eV for BiOCl; Fig. S3†). However, when Bi_4NbO_8Cl and Bi_2GdO_4Cl are compared, the oxygen site in the latter is much more destabilized by the $2NNL_d$ (−40.0 eV of Bi_2GdO_4Cl *vs.* −20.3 eV of Bi_4NbO_8Cl) as shown in Fig. 2. For this reason, the electrostatic potentials from several sublayers for Bi_2GdO_4Cl and hypothetical Bi_4NbO_8Cl were calculated using the square-prism model with $A = 200$ Å (Fig. 2). It is seen that while the BL, 1NNLs and $2NNL_u$ of the two compounds generate nearly the same electrostatic potential, the electrostatic potential of Bi_2GdO_4Cl from the $2NNL_d$ is almost twice as large as that of Bi_4NbO_8Cl. Although the $2NNL_d$ in both compounds has an oxygen square network, their densities are different, with the formal charges of $[O_2]^{4-}$ in Bi_2GdO_4Cl and $[O]^{2-}$ in Bi_4NbO_8Cl. Importantly, this model shows the crucial contribution from the 3NNL. Since the $3NNL_u$ of both compounds is composed of the $[Bi]^{3+}$ sublayer (Fig. 1), there is little difference in electrostatic potential. On the other hand, the $3NNL_d$ of Bi_4NbO_8Cl consists of a Nb square network ($d_{Nb-Nb} = 3.9$ Å $= a$) and O square network ($d_{O-O} = 2.7$ Å $= 1/\sqrt{2}a$), while that of Bi_2GdO_4Cl consists of a Bi square network ($d_{Bi-Bi} = 3.9$ Å), giving electrostatic potentials of 662 eV and 1935 eV, respectively. These values are again correlated with the formal charges of $[NbO_2]^+$ and $[Bi]^{3+}$. Accordingly, stabilization of Bi_4NbO_8Cl (*vs.* Bi_2GdO_4Cl) by the $2NNL_d$ is compensated by destabilization by the $3NNL_d$, which accounts for the similar values of Madelung site potential in these compounds. The present results demonstrate that 3NNLs have a substantial impact on the Madelung potential at the oxygen site in the BL, thereby affecting the valence band structures.

Let us briefly discuss the influence of halogen anions on Madelung potential by comparing the isostructural series, BiOX or Bi_2GdO_4X (X = Cl, Br, I). The Madelung site potential of BiOX increases with increasing the ionic radius of X, r_X, whereas that of Bi_2GdO_4X hardly changes (Fig. S1†). This results from highly anisotropic lattice expansion (Table S4†); $\Delta c/\Delta a$ is 16.2 for BiOX and 13.2 for Bi_2GdO_4X, where Δa and Δc are the differences in the lattice constant between X = Cl and I. The evolution of the interlayer distance is more pronounced for Bi–X and X–X (Fig. S6†). In particular, the X–X distance in BiOX (2NNLs and 3NNLs) remarkably changes with X. It is then likely that the predominant expansion electrostatically stabilizes the oxygen layer (BL), indicating that a double halogen layer can be used to tune the Madelung site potential.

Now that we possess a tool (square-prism model) that can evaluate the impact of distant sublayers, we are ready to apply the square-prism model to other layered compounds. This model was applied to $Sr_3Sc_2Cu_2S_2O_5$ and $Sr_2ScCuSO_3$ with the antifluorite Cu_2S_2 layer as shown in Fig. 7a. They show excitonic luminescence properties, which can be tuned by the composition and stacking pattern.[30] $Sr_3Sc_2Cu_2S_2O_5$ is also a promising p-type transparent conductor due to its high conductivity and a large band gap.[24] The Madelung potential at the sulfur site (BL) for $Sr_3Sc_2Cu_2S_2O_5$ is 17.0 eV, which is smaller than 18.2 eV for $Sr_2ScCuSO_3$. As shown in Fig. 7b, sublayers up to 3NNLs and $4NNL_u$ are common to the two compounds and thus give nearly the same electrostatic potential. The smaller Madelung potential of $Sr_3Sc_2Cu_2S_2O_5$ can be attributed to the smaller electrostatic potential from the $4NNL_d$ sublayer in $Sr_3Sc_2Cu_2S_2O_5$

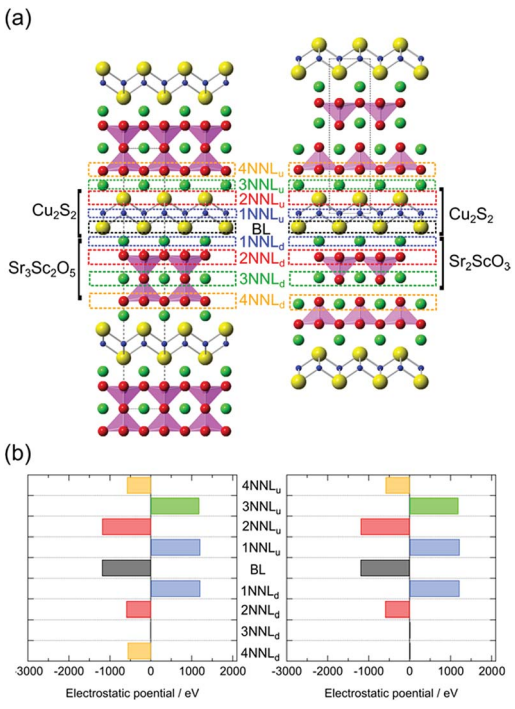

Fig. 7 (a) Crystal structures of $Sr_3Sc_2Cu_2S_2O_5$ (left) and $Sr_2ScCuSO_3$ (right) with antifluorite-derived Cu_2S_2 layers. The S layer and its neighboring sublayers (*n*-th nearest-neighbor layer; *n*NNL) are indicated. Blue, yellow, green and red spheres, respectively, represent Cu, S, Sr and O atoms, and ScO_5 pyramids are shown in pink. (b) Electrostatic potential at the sulfur site in the Cu_2S_2 layer from adjacent sublayers calculated using the square-prism model with $A = 200$ Å.

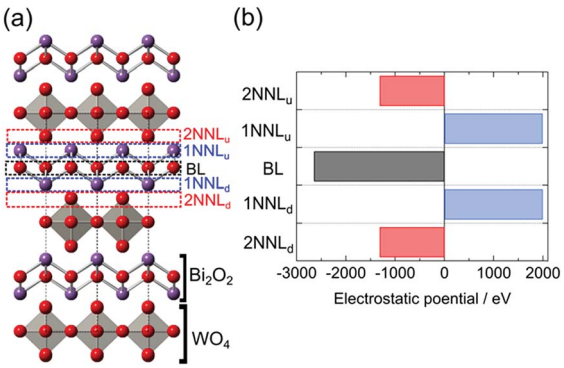

Fig. 8 (a) The non-distorted structure of Bi_2WO_6. The fluorite-derived basal layer (BL) and its neighboring sublayers (*n*-th nearest-neighbor layer; *n*NNL) are indicated. Purple and red spheres represent Bi and O atoms, respectively. (b) Electrostatic potential at the oxygen site of Bi_2WO_6 in the fluorite-type (BL) layer from adjacent sublayers calculated using the square-prism model with $A = 200$ Å.

composed of $[ScO_2]^-$ compared with that of the $4NNL_d$ in $Sr_2ScCuSO_3$ composed of $[SrO]^0$ sublayers.

Bi_2WO_6, a visible-light responsive photocatalyst,[36] has a layer stacking similar to that of Bi_4NbO_8Cl with fluorite-type Bi_2O_2 and perovskite-type WO_4 layers, but the halogen layer is absent (Fig. 8a). The Madelung potential at the oxygen site in the Bi_2O_2 layer is 14.9 eV on average, which is much smaller than that of Bi_4NbO_8Cl (18.2 eV). The L^2MP analysis using a hypothetical non-distorted lattice (Fig. 8b) shows that the difference arises from a smaller electrostatic potential from the $[O]^{2-}$ sublayer in the $2NNL_u$ (*vs.* the $[Cl]^-$ sublayer in Bi_4NbO_8Cl). Thus, one expects a lower VBM for Bi_2WO_6. However, the experimentally obtained VBM of Bi_2WO_6 of 2.68 V (*vs.* SHE at pH 2.0) is much lower than that of Bi_4NbO_8Cl of 2.27 V.[12] Such a discrepancy implies that there are other factors, such as the hybridization effect between Bi 6s orbitals and O 2p orbitals, which has been shown to be quite strong in Bi_4NbO_8Cl.[16]

Conclusions

We investigate the influence of distant sublayers on Madelung site potential by developing an alternate model for L^2MP analysis and applying it to Bi_2O_2-based oxyhalide photocatalysts (BiOX, Bi_2GdO_4X and Bi_4NbO_8X) and other layered materials. Among the two models examined, the square-prism model shows better convergence. A significant contribution of electrostatic potential from the 3NNL explains nearly the same Madelung site potential between Bi_2GdO_4Cl and Bi_4NbO_8Cl. In addition, a strong X dependence of the Madelung site potential is observed in BiOX. The L^2MP analysis of Bi_2WO_6, $Sr_3Sc_2Cu_2S_2O_5$ and $Sr_2ScCu_SO_3$ further revealed a distant layer contribution to the Madelung site potential. Given the enormous variations of composition and layer stacking sequences in layered oxyhalides and more generally mixed-anion compounds,[37] L^2MP analysis offers large potential for the prediction and tuning of desired valence band structures for photocatalytic applications and other functions, possibly with the aid of a machine learning approach.

Conflicts of interest

The authors declare no competing financial interest.

Acknowledgements

This work was supported by the Grant-in-Aid for Scientific Research on Innovative Areas "Mixed Anion" project (JP16H06439, JP16H06440, and JP16H06441) from MEXT and CREST (JPMJCR1421).

References

1 P. A. Cox, *The Electronic Structure and Chemistry of Solids*, Oxford University Press, Oxford, United Kingdom, 1986.
2 A. H. Kahn and A. J. Leyendecker, *Phys. Rev.*, 1964, **135**, A1321–A1325.
3 J. D. Levine and S. Freeman, *Phys. Rev. B: Solid State*, 1970, **2**, 3255–3272.
4 J. B. Torrance and R. M. Metzger, *Phys. Rev. Lett.*, 1989, **63**, 1515–1518.
5 Y. Ohta, T. Tohyama and S. Maekawa, *Phys. Rev. Lett.*, 1991, **66**, 1228–1231.
6 Y. Ohta, T. Tohyama and S. Maekawa, *Phys. Rev. B: Condens. Matter Mater. Phys.*, 1991, **43**, 2968–2982.
7 I. Hase and T. Yanagisawa, *Phys. Rev. B: Condens. Matter Mater. Phys.*, 2007, **76**, 174103.
8 A. Walsh, *Appl. Phys. Lett.*, 2011, **98**, 261910.
9 D. O. Scanlon, C. W. Dunnill, J. Buckeridge, S. A. Shevlin, A. J. Logsdail, S. M. Woodley, C. R. Catlow, M. J. Powell, R. G. Palgrave, I. P. Parkin, G. W. Watson, T. W. Keal, P. Sherwood, A. Walsh and A. A. Sokol, *Nat. Mater.*, 2013, **12**, 798–801.
10 J. Buckeridge, K. T. Butler, C. R. A. Catlow, A. J. Logsdail, D. O. Scanlon, S. A. Shevlin, S. M. Woodley, A. A. Sokol and A. Walsh, *Chem. Mater.*, 2015, **27**, 3844–3851.
11 H. Fujito, H. Kunioku, D. Kato, H. Suzuki, M. Higashi, H. Kageyama and R. Abe, *J. Am. Chem. Soc.*, 2016, **138**, 2082–2085.
12 H. Kunioku, M. Higashi, C. Tassel, D. Kato, O. Tomita, H. Kageyama and R. Abe, *Chem. Lett.*, 2017, **46**, 583–586.
13 H. Suzuki, H. Kunioku, M. Higashi, O. Tomita, D. Kato, H. Kageyama and R. Abe, *Chem. Mater.*, 2018, **30**, 5862–5869.
14 A. Nakada, A. Saeki, M. Higashi, H. Kageyama and R. Abe, *J. Mater. Chem. A*, 2018, **6**, 10909–10917.
15 D. Kato, K. Hongo, R. Maezono, M. Higashi, H. Kunioku, M. Yabuuchi, H. Suzuki, H. Okajima, C. Zhong, K. Nakano, R. Abe and H. Kageyama, *J. Am. Chem. Soc.*, 2017, **139**, 18725–18731.
16 H. Kunioku, M. Higashi, O. Tomita, M. Yabuuchi, D. Kato, H. Fujito, H. Kageyama and R. Abe, *J. Mater. Chem. A*, 2018, **6**, 3100–3107.
17 D. O. Charkin, *Russ. J. Inorg. Chem.*, 2008, **53**, 1977–1996.
18 Y. Tokura and T. Arima, *Jpn. J. Appl. Phys., Part 1*, 1990, **29**, 2388–2402.
19 Y. Kamihara, T. Watanabe, M. Hirano and H. Hosono, *J. Am. Chem. Soc.*, 2008, **130**, 3296–3297.
20 K. Tanabe and H. Hosono, *Jpn. J. Appl. Phys.*, 2012, **51**, 010005.
21 Y. Mizuguchi, *J. Phys. Soc. Jpn.*, 2019, **88**, 041001.
22 J. B. Goodenough and K. S. Park, *J. Am. Chem. Soc.*, 2013, **135**, 1167–1176.
23 K. Ueda, S. Inoue, S. Hirose, H. Kawazoe and H. Hosono, *Appl. Phys. Lett.*, 2000, **77**, 2701–2703.
24 M. L. Liu, L. B. Wu, F. Q. Huang, L. D. Chen and I. W. Chen, *J. Appl. Phys.*, 2007, **102**, 116108.
25 A. M. Kusainova, S. Y. Stefanovich, V. A. Dolgikh, A. V. Mosunov, C. H. Hervoches and P. Lightfoot, *J. Mater. Chem.*, 2001, **11**, 1141–1145.
26 M. Schmidt, H. Oppermann, C. Hennig, R. W. Henn, E. Gmelin, N. Soger and M. Binnewies, *Z. Anorg. Allg. Chem.*, 2000, **626**, 125–135.
27 K. G. Keramidas, G. P. Voutsas and P. I. Rentzeperis, *Z. Kristallogr.–Cryst. Mater.*, 1993, **205**, 35–40.

28 J. Ketterer and V. Kramer, *Acta Crystallogr., Sect. C: Cryst. Struct. Commun.*, 1986, **42**, 1098–1099.
29 K. Otzschi, H. Ogino, J. Shimoyama and K. Kishio, *J. Low Temp. Phys.*, 1999, **117**, 729–733.
30 H. Ogino, J. Shimoyama, K. Kishio, Y. Katsura, M. Tsuboi, K. Yamanoi, M. Cadatal-Raduban, T. Nakazato, T. Shimizu and N. Sarukura, *Appl. Phys. Lett.*, 2012, **101**, 191901.
31 H. Okudera, Y. Sakai, K. Yamagata and H. Takeda, *Acta Crystallogr., Sect. B: Struct. Sci., Cryst. Eng. Mater.*, 2018, **74**, 295–303.
32 S. J. Clark, M. D. Segall, C. J. Pickard, P. J. Hasnip, M. J. Probert, K. Refson and M. C. Payne, *Z. Kristallogr.–Cryst. Mater.*, 2005, **220**, 567–570.
33 J. Perdew, A. Ruzsinszky, G. Csonka, O. Vydrov, G. Scuseria, L. Constantin, X. Zhou and K. Burke, *Phys. Rev. Lett.*, 2008, **100**, 136406.
34 K. Momma and F. Izumi, *J. Appl. Crystallogr.*, 2011, **44**, 1272–1276.
35 H. M. Evjen, *Phys. Rev.*, 1932, **39**, 675–687.
36 A. Kudo and S. Hijii, *Chem. Lett.*, 1999, **28**, 1103–1104.
37 H. Kageyama, K. Hayashi, K. Maeda, J. P. Attfield, Z. Hiroi, J. M. Rondinelli and K. R. Poeppelmeier, *Nat. Commun.*, 2018, **9**, 772.